A Hybrid Computational and Analytical Model of Inline Drip Emitters

Jaya Narain[1]

Global Engineering and Research Laboratory,
Department of Mechanical Engineering,
Massachusetts Institute of Technology,
Cambridge, MA 02139-4306
e-mail: jnarain@mit.edu

Amos G. Winter V

Global Engineering and Research Laboratory,
Department of Mechanical Engineering,
Massachusetts Institute of Technology,
Cambridge, MA 02139
e-mail: awinter@mit.edu

This paper details a hybrid computational and analytical model to predict the performance of inline pressure compensating drip irrigation emitters. Pressure compensating emitters deliver a constant flow rate over a range of applied pressures to accurately meter water to crops. Flow rate is controlled within the emitter via a fixed resistance tortuous path, and a variable flow resistance composed of a flexible membrane that deflects under changes in pressure, restricting the flow path. A pressure resistance parameter was derived using an experimentally validated computational fluid dynamics (CFD) model to describe the flow behavior in tortuous paths. The bending mechanics of the membrane were modeled analytically and refined by deriving a correction factor using finite element analysis (FEA). A matrix formulation that calculates the force applied by a line or a patch load of any shape on a rectangular membrane, along which there is a prescribed deflection, was derived and was found to be accurate to be 1%. The combined hybrid computational–analytical model reduces the computational time of modeling emitters from hours to less than 30 min, dramatically lowering the time required to iterate and select optimal designs. The model was validated experimentally using three commercially available drip emitters and was accurate to within 12% of the experimental results.
[DOI: 10.1115/1.4042613]

1 Introduction

This paper presents a hybrid computational and analytical model of inline drip emitters that predicts the flow rate of an inline emitter as a function of pressure, given an input geometry. Drip irrigation is a method of irrigation that delivers a steady, controlled flow of water directly to the roots of a plant. The emitters in the drip system regulate the water flow rate, ensuring that each crop in a field gets approximately the same amount of water. This method of irrigation reduces water consumption by preventing drainage and evaporation and can generate significant yield improvements over conventional methods of irrigation. A study conducted in India showed water savings between 20% and 40% and increases in yield between 20% and 50% with drip irrigation compared to that with furrow (flood) irrigation, depending on the crop grown [1]. Drip irrigation can enable farmers to grow crops under conditions where they could not otherwise do so (e.g., with strict water constraints or in dry seasons), allow farmers to grow a wider array of crops, and save on labor and fertilizer costs [2]. Solar-powered drip irrigation systems generally require low-pressure drip systems to minimize pumping power (which is the product of pressure and flow rate) [3,4]. Reducing the activation pressure of drip emitters can significantly decrease the energy consumption of a drip irrigation system, lowering the capital cost of a solar-powered drip irrigation system [5], particularly for farms with surface water sources.

This paper focuses on inline drip emitters (Fig. 1), which are embedded inside pipes. Pipes are sold based on emitter spacing and flow rate depending on the crop type and spacing. In contrast, online emitters are sold separately from piping and must be installed by inserting them into the exterior of the pipe one at a time. Because inline drip emitters do not require individual installation, they are generally more popular than online emitter types and account for the significant majority of drip emitter sales [6].

Emitters can be described as pressure compensating (PC) or nonpressure compensating (NPC). PC drip emitters deliver a relatively constant flow rate over a wide range of pressures. The activation pressure is defined as the pressure at which the desired flow rate and flow-compensating behavior begins (Fig. 2). Individual emitters are characterized by their activation pressure (for PC emitters), nominal rated flow rate, and the variation in flow rate from the nominal value. PC drip emitters typically consist of a tortuous flow path and a flexible membrane that deforms to control the flow resistance (Figs. 3(a) and 3(b)). The deformation of the membrane depends on the relative magnitudes of the input pressure, the pressure underneath the membrane, and atmospheric pressure. In PC drippers, the design of the tortuous path affects the activation pressure by affecting the pressure differential acting on the membrane, and thus the pressure at which the membrane makes contact with the lands (Fig. 3(c)). The net pressure acting on the membrane is the difference between the water pressure on top of the membrane and the pressure underneath the membrane.
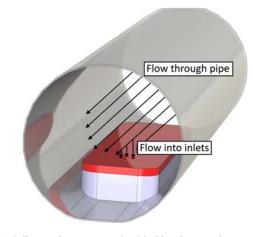

Fig. 1 Inline emitters are embedded in pipes at the manufacturing stage. Water moves from the pipe into the emitter inlet.
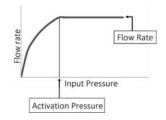

Fig. 2 Ideal pressure compensating behavior. The flow rate through the emitter is a function of two primary flow resistances: the tortuous path and the membrane deforming into the channel and lands (Fig. 3). As the input pressure over the membrane increases, the resistance through the channel also increases, resulting in a proportionally lower flow rate. The pressure compensating mechanism caused by variable flow resistance leads to a constant flow rate at pressures higher than the activation pressure of the emitter.
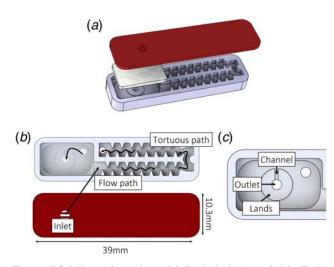

Fig. 4 NPC inline drip emitter. (*a*) NPC emitters consist of an array of inlets leading to a tortuous path. (*b*) The emitter is bonded to the inside of the lateral pipe to seal the tortuous path. (*c*) The external surface of a lateral pipe with an NPC emitter bonded to the inside.

Fig. 3 PC inline drip emitter. (*a*) Exploded view of Jain Turbo Cascade 2 l/h inline drip emitter showing the two injection molded parts that sandwich a silicone membrane. (*b*) Water from the inlet flows to the start of the tortuous path, through the tortuous path, and into a rectangular chamber that has a small channel that provides passageway though circular lands. A silicone membrane rests on the top of the rectangular chamber that deforms under pressure to limit the flow. (*c*) After the membrane has touched the lands, water must flow through the channel in the lands to reach the outlet.

The pressure underneath the membrane includes both the water pressure of flow exiting the tortuous path and the atmospheric pressure, which acts on the portion of the membrane directly above the outlet. The tortuous path also plays a role in determining the nominal flow rate of the emitter. NPC drip emitters typically consist solely of a tortuous flow path (Fig. 4) and thus have a fixed flow resistance. The design of the tortuous path dictates the flow rate behavior as a function of pressure for an NPC emitter [7].

Understanding the flow behavior through tortuous paths, as well as the coupled fluid-solid mechanics of the flow restriction caused by the deformation of flexible membrane, can be used to design improved emitter technologies. Palau-Salvador et al. [8] showed that computational fluid dynamics (CFD) could be used to accurately simulate flow through tortuous paths in inline emitters. Previous studies on the tortuous path behavior have used CFD as a tool to analyze the effects of altering dentate geometry in flow paths [9]. Wei et al. [10] used CFD to characterize the effect of rectangular, trapezoidal, and triangle labyrinth geometries. CFD models, while accurate, can require significant user input to make robust changes to complex geometric structures. CFD models of emitters
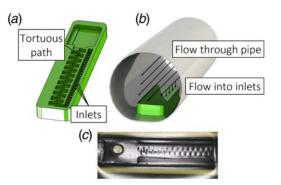
with labyrinth flow paths and coupled fluid–structure interactions (FSIs) require significant computational power and time. For example, a FSI simulation of an aortic valve with 500,000 tetrahedral elements had a run time of 145.5 hours [11]. Simulations of smaller valves with 43,008–81,920 brick elements required 13–90 h, depending on the loading conditions and valve layout [12]. The size of the flexible component in the emitter is smaller than the size of the flexible component in the large valve, but the fluid domain is significantly larger. Based on the cited literature on FSI models and small test simulations, it was estimated that an FSI simulation of a drip emitter would have a run time of at least 24 h.

Some full models of pressure compensating emitter behavior exist in the literature. Shamshery et al. [13] analytically modeled the pressure versus the flow rate behavior of circular PC online emitters that use an orifice rather than a tortuous path for inlet restriction. Zhengying [14] modeled cylindrical inline emitters with high accuracy using computational FSI methods. Wang et al. [15] used FSI to model the behavior of circular online drip emitters with high accuracy. The purely analytical model published by Shamshery et al. [13,5] has very low computational time, but average errors of approximately 40% when applied to 3.3 and 4.2 l/h emitters, which require an additional fitting function to resolve [5].

This paper provides a quantitative description of inline PC drip emitter performance, as well as computational and design tools that will enable irrigation engineers to quickly iterate designs. This parametric design theory may lead to improved designs with a lower activation pressure, which can reduce the pumping power. The model described in this paper has higher fidelity than analytical models described in the literature and requires lower computational time than a fully numerical FSI model of a PC drip emitter. This model includes a verified CFD model to predict the flow behavior through tortuous paths; a method of extracting a pressure scaling parameter from the CFD results to be used in an analytical model; analytical expressions that describe the bending of asymmetric rectangular membranes in inline drip emitters; finite element analysis (FEA) on the interaction between the membrane and lands to characterize the total flow resistance through the emitter; and analytical expressions that describe the fluid mechanics of internal flows, used to predict the net flow rate out of the emitter. The resulting hybrid computational and analytical model was verified using three distinct, commercially available emitter geometries.

The presented model is capable of parametrically describing emitter designs with various flow path architectures. The model also benefits from both the accuracy of computational methods for characterizing complex flow paths and nonlinear mechanics and the processing speed attainable with analytical expressions.

2 CFD Model of Flow Through Tortuous Path

This section describes how CFD was utilized to predict the pressure drop caused by the tortuous path and to determine the corresponding loss coefficient. Both the PC and NPC drip emitters investigated in this study use a tortuous path as a flow restrictor. NPC emitters (Fig. 4(a)), which consist of only an inlet system and a tortuous flow path, were used to verify the capability of the CFD model to provide accurate results. Three model geometries were investigated, consisting of single drip emitters with tortuous flow path dimensions equivalent to those of Jain Turbo Excel Plus 0.75, 1.6, and 4 l/h emitters, which are commercially available products made by Jain Irrigation Ltd. (Jalgaon, India). These flow rates were selected because they span the range of typical flow rates for NPC drip emitters and have distinct flow paths. The flow behavior was modeled using the ANSYS CFX 16.0 package.

In NPC drippers, the tubing itself provides a part of the wall that bounds the flow through the tortuous path (Figs. 4(b) and 4(c)). A fine, controlled mesh was used at the interfaces between the fluid and emitter walls, and between the fluid and piping, to capture the large gradients in flow properties characteristic of boundary layers. The walls were modeled as smooth. A minimum element size on the faces of the fluid in contact with the dripper of 1.8×10^{-4} m was used to ensure a mesh sufficiently fine to capture the flow behavior. Test runs with smaller element sizes converged yielding the same results as runs with the cited element size. The simulated fluid domain had between 970,974 and 997,247 tetrahedral elements depending on the geometry of the modeled emitter. A shear stress transport (SST) model was used for turbulence as it is suitable for cases in which flow separation and recirculating regions in the flow path are expected [16].

A boundary condition of total pressure was set at the pipe inlet. Total pressure represents the pressure in the irrigation pipe before the flow enters the emitter and was used as an independent variable. The inlet flow was defined as normal to the pipe inlet with a medium turbulence turbulent intensity of 5%. A boundary condition of average atmospheric static pressure of zero gauge pressure was set at the emitter outlet.

To bond inline emitters to polythylene tubing at the manufacturing facility of Jain Irrigation Ltd., polyethylene tubing is heat-formed around a moving line of inline emitters. The heat formation process creates a bond between the inside surface of the tubing and the body of each inline emitter. In NPC emitters, the heat-forming process results in portions of the tubing being pushed into the tortuous path, altering the flow path dimensions (Fig. 4(c)). This obstruction was modeled as a 1.5×10^{-4} m reduction in the depth of the tortuous path, based on measurements on Jain emitters embedded in pipes.

A visualization of the flow through the emitter as computed by the CFD model (Fig. 5) is consistent with images published by Jain Irrigation Ltd.[2] and Wei et al. [10]. The bulk of the flow moves through the center of the flow path. Lower velocity recirculation zones are formed in the teeth of the labyrinth. Studies on other labyrinth channels have found that recirculation zones affect the likelihood of emitter clogging [10]. The affect may be positive or negative depending on the strength and location of the recirculating zone.

Results of the CFD model were compared to measure emitter flow rates under controlled pressures for the 0.75, 1.6, and 4 l/h Turbo Excel Plus driplines (Fig. 6). The pressure was measured in the pipe near the inlet of the dripper using a Dwyer DPGA Series digital pressure gauge (±0.1 bar). The flow rate out of the dripline was measured using a graduated cylinder (±3 ml) and timer (±3 s). Figure 6 also shows the geometry of each emitter and reports the 95% confidence interval for the experimental measurements. The flow rate behavior as a function of pressure predicted by the CFD

Fig. 5 Velocity vectors along the flow path through an NPC drip emitter rated at 1.6 l/h, computed using ANSYS CFX. Flow enters the emitter through a row of rectangular inlets that lead directly to the tortuous path.
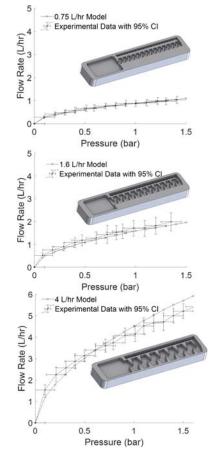

Fig. 6 Flow rate as a function of pressure predicted by the CFD model (solid line with circles) compared to the experimental data (dashed line with crosses) for three NPC emitters. The CAD model shown with each plot is of the corresponding emitter.

model reliably overlapped with the 95% confidence interval of the experimental data, validating the CFD model predictions.

The Re number in the paths varies from 75 to 800, depending on the emitter geometry and input pressure. Nishimura and Matsumoto [17] found that transition to turbulence occurred in sinusoidal channels at Re numbers between 200 and 350. Dai et al. [18] found that the transition number in zigzag channels is highly dependent on the channel geometry. Based on the calculated Re numbers, it was expected that the flow was largely in the turbulent regime. Some measured points may correspond to the laminar flow because of the sensitivity of the transition point on geometry and the wide range of flow rates studied. However, the experimental validation (Fig. 6) showed the relationship between pressure drop and flow rate—the variables used in the hybrid model presented herein—which was predicted accurately for a wide range of flow rates and geometries. As such, modeling the flow in the tortuous path as turbulent was deemed to be sufficient.

3 Scaling Parameter Based on Tortuous Path Geometry

The primary objective of this paper is to develop an accurate, computationally efficient model of PC emitters. It is difficult to experimentally verify a CFD model of tortuous paths in PC emitters directly because the overall flow behavior is influenced by both the tortuous path and the silicone membrane pressure compensating mechanism (Fig. 3). Therefore, these two flow resistances were investigated separately. The tortuous path resistance is described in this section. A CFD model that accurately predicts the flow behavior for NPC emitters can be extended to the tortuous path in PC emitters because the design of tortuous paths and the placement of the path in the overall emitter architecture are similar between NPC and PC emitters (Figs. 3 and 4). Therefore, the verified tortuous path CFD model was used to characterize flow resistance through tortuous paths equivalent to those in Jain PC Turbo Cascade 1.1, 2, and 3.8 l/h emitters.

The flow through the tortuous path is expected to be turbulent for the majority of the pressure range studied. As such, the flow rate Q can be expressed as a function of the pressure drop $P_2 - P_1$ through the path and a flow resistance parameter K_1 by

$$Q = \sqrt{\frac{P_2 - P_1}{K_1}} \qquad (1)$$

where P_1 is the pressure at the inlet of the emitter and P_2 is the pressure at the end of the tortuous path. For a PC emitter, where there is a second pressure drop caused by the silicone membrane pressure compensating mechanism (Fig. 7), P_2 can be calculated iteratively using Eq. (1) and

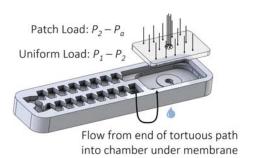$$P_2 - P_a = \frac{1}{2}(\rho)(K_{mt})Q^2 \qquad (2)$$

Fig. 7 Membrane loading in a PC drip emitter. Water enters the dripper at pressure P_1, flows through the tortuous path and drops to pressure P_2, and then flows into the rectangular chamber underneath the membrane, over the lands and through the channel, and out to atmospheric pressure P_a. The pressure differential applied to the membrane causes it to deflect and control the flow resistance.
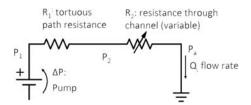
Fig. 8 The flow rate through a PC emitter is a function of two primary flow resistances: the tortuous path and the membrane interaction with the channel and the lands. As P_1 increases, the resistance through the channel R_2 also increases, resulting in a proportionally lower flow rate.

Table 1 Summary of average tortuous path flow resistances K_1 and standard deviations calculated using CFD simulation results for 16 input pressures for each PC inline emitter path geometry

Emitter flow rate (l/h)	Average K_1 [(Pa h^2)/l^2]	Standard deviation [(Pa h^2)/l^2]
3.8	2428	77
2	3245	36
1.1	3239	48

where P_a is the atmospheric pressure at the dripper outlet, K_{mt} is the total flow resistance under the membrane, and ρ is the density of water, taken as 1000 kg/m^3. The procedure for determining K_{mt} is discussed later in this paper. The process for calculating P_2 is analogous to using the voltage divider rule in an electrical circuit (Fig. 8), given the total applied potential (in this case $P_1 - P_a$) and the resistance of two resistors in series.

To measure P_2, a virtual sensor was placed at the end of the tortuous path in the CFD model, immediately before entering the PC chamber with the channel and lands. The simulation was run for 16 distinct values of P_1, ranging from 0.1 to 1.6 bar, for each path geometry. The calculated tortuous path flow resistance and the corresponding standard deviation for each emitter geometry are summarized in Table 1. It was found that the tortuous path resistance K_1 depends primarily on the geometry of the tortuous path; it does not vary significantly with the pressure potential applied over the path $P_1 - P_2$ or flow rate Q. The K_1 parameter is expected to have low sensitivity to pressure based on the simulation and experimental results presented, given that the flow is primarily in the turbulent regime.

The standard deviations of the tortuous path resistance were very small compared to the average values. The K_1 value for the 3.8 l/h emitter was the lowest. This means that the pressure drop in the tortuous path in the 3.8 l/h emitter is less than the pressure drop in the paths in the 2 and 1.1 l/h emitters. This result was expected because the path in the 3.8 l/h emitter is wider and has fewer turns than the paths in other emitters. Despite differences in the path geometry, the scaling factors for the 2 and 1.1 l/h emitters were nearly identical. Although the 2 l/h emitter has a wider flow path and fewer turns than the 1.1 l/h emitter, it had significantly more recirculating flow than the 1.1 l/h emitter. Dai et al. found that vortices and flow separation near bends in tortuous channels lead to higher pressure drops [18]. This phenomenon would account for similar tortuous path resistances for the 1.1 and 2 l/h flow paths despite distinct geometries.

K_1 can be reliably determined by simulating the flow at only one input pressure because the standard deviation between measurements is small. A single value of K_1 can then be used to model the total flow behavior of an emitter. Traditionally, the flow behavior through a tortuous path is characterized by fitting complex polynomial or exponential functions to a curve of flow rate as a function of pressure [14,19]. Generating a full curve requires significantly more computational time than simulating the flow at only a single point.

4 Description of Pressure Compensating Behavior

In a PC emitter, after passing through the tortuous path, the flow enters into the pressure compensating chamber underneath a silicone membrane (Fig. 7). To pass from the tortuous path into the chamber, the flow moves through a passage between the emitter and pipe that connects the end of the tortuous path to the chamber underneath the membrane.

Due to the tortuous path, the water enters the chamber underneath the membrane at a pressure P_2, which is lower than the input pressure P_1 above the membrane (Fig. 7). The outlet is open to the atmospheric pressure P_a. The resulting pressure differentials across the membrane cause it to deflect (Fig. 9). As P_1 increases, the membrane deflects farther and farther into the chamber until it hits the lands at pressure P_L. For pressures greater than P_L, the flow must move through the small channel that passes through the lands to reach the emitter outlet (Fig. 3(c)).
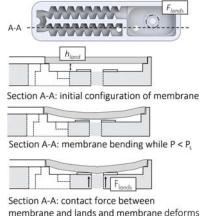
The increasing flow resistance as the membrane deflects causes the pressure P_2 under the membrane to increase. The pressure drop through the channel $P_2 - P_a$ increases as P_1 increases. An increase in flow resistance through the channel regulates the flow rate as $P_2 - P_a$ increases.

In the physical devices, the membrane has an initial curvature caused by a protrusion on the cap of the emitter. In the model, the distance between the membrane and the lands was estimated as the distance between the center of the membrane and the lands.

After the membrane touches the lands, the lands apply a contact force on the membrane. For $P_1 > P_L$, the membrane deforms into the channel. The magnitude of obstruction is primarily a function of the input pressure P_1. At higher input pressure, the magnitude of deformation is greater, leading to a higher flow resistance in the channel. The emitter pressure compensates because the flow resistance is greater for higher input pressure—i.e., for a range of pressures beginning with the activation pressure P_{act}, water leaves the emitter at a constant flow rate (Fig. 2).

4.1 Membrane Bending for $P_1 < P_L$.
Before the membrane touches the lands, the loading on the membrane can be modeled as the linear superposition of a uniform load and a patch load (Fig. 10). The pressure P_1 is applied uniformly over the top surface of the membrane. In regions where there is fluid of pressure P_2 beneath the membrane, the loading is $P_1 - P_2$. In regions where there is no fluid at P_2 beneath the membrane, the loading is $P_1 - P_a$. This loading can be represented by the superposition of a uniform load $P_1 - P_2$ over the entire membrane and a patch load $P_2 - P_a$ over the portion of the membrane that is not in contact with the fluid at pressure P_2 (Fig. 7).

The membrane was modeled as a rectangular plate with four simply supported edges. The dimensions of the membrane were taken as the distances between each set of parallel supports. The membrane was modeled after the membranes used in the 1.1, 2, and 3.8 l/h Turbo Cascade emitters, which have a length a of 7.0 mm, a width b of 12.0 mm, and a thickness h of 1.2 mm. All emitter dimensions given in this paper were measured using hand calipers (± 0.1 mm).

Fig. 9 Cross-sectional view of the pressure compensating chamber in an inline drip emitter
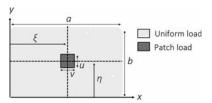

Fig. 10 Loading on membrane for $P_1 < P_L$. Before the membrane touches the lands, the loading on the membrane can be modeled as the superposition of a uniform load and a patch load.

The material properties of the membrane were found using correlation between material properties and material hardness for rubbers [20]. To find the hardness of the membrane, the procedure described in ASTM 2240 [21] was used with a type A durometer. A stack of membranes were used to achieve the necessary specimen thickness. The measurement process was repeated three times, and it was found that the membrane had a hardness of 52 ± 1 Shore A.

The Young's modulus E of a rubber in megapascal is related to the Shore A hardness H_A by [20]

$$E = (15.75\,\text{MPa} + 2.15\,\text{MPa} \times H_A)/(100 - H_A). \qquad (3)$$

This expression gives a Young's modulus E of 2.66 ± 0.18 MPa. For a neo-Hookean material, the shear modulus G is one-third of E, 0.89 MPa. By using these values of E and G, the Poisson's ratio of the membrane ν was calculated to be 0.488 [20].

The deflection of the membrane due to the uniform load $w_{uniform}$ can be modeled using a Navier double series solution [22],

$$w_{uniform}(x, y) = \frac{16(P_1 - P_2)}{D\pi^6}\left(\frac{\sin\frac{\pi x}{a}\sin\frac{\pi y}{b}}{\left(\frac{1}{a^2}+\frac{1}{b^2}\right)^2} + \frac{\sin\frac{3\pi x}{a}\sin\frac{\pi y}{b}}{3\left(\frac{9}{a^2}+\frac{1}{b^2}\right)^2} + \frac{\sin\frac{\pi x}{a}\sin\frac{3\pi y}{b}}{3\left(\frac{1}{a^2}+\frac{9}{b^2}\right)^2} + \frac{\sin\frac{3\pi x}{a}\sin\frac{3\pi y}{b}}{9\left(\frac{9}{a^2}+\frac{9}{b^2}\right)^2} \right) \qquad (4)$$

where D is the flexural modulus of the membrane and is given by

$$D = \frac{Eh^3}{12(1-\nu^2)} \qquad (5)$$

The portion of the membrane that is not in contact with the fluid at pressure P_2 becomes larger as P_1 increases beyond P_L, and the

contact area between the membrane and the lands increases. This is because there is no fluid flow under the membrane in regions where the membrane is in contact with the lands. To approximate this effect, the area of application of the patch load was approximated as the average lands diameter or half the distance between the inner and outer lands. Although the emitter outlet and lands

are circular, the patch was approximated as a rectangular patch of the same area as the average lands diameter because the membrane is rectangular and calculations were done in Cartesian coordinates

(Fig. 10). The deflection of the membrane due to the patch load w_{patch} can also be modeled using a Navier double series solution [22],

$$w_{patch}(x, y) = \frac{16(P_1 - P_2)}{D\pi^6} \times \left(\frac{\sin\frac{\pi\eta}{a}\sin\frac{\pi\xi}{b}\sin\frac{\pi u}{2a}\sin\frac{\pi b}{2b}\sin\frac{\pi x}{a}\sin\frac{\pi y}{b}}{\left(\frac{1}{a^2} + \frac{1}{b^2}\right)^2} + \frac{\sin\frac{3\pi\eta}{a}\sin\frac{\pi\xi}{b}\sin\frac{3\pi u}{2a}\sin\frac{\pi b}{2b}\sin\frac{3\pi x}{a}\sin\frac{\pi y}{b}}{3\left(\frac{9}{a^2} + \frac{1}{b^2}\right)^2} \right.$$

$$\left. + \frac{\sin\frac{\pi\eta}{a}\sin\frac{3\pi\xi}{b}\sin\frac{\pi u}{2a}\sin\frac{3\pi b}{2b}\sin\frac{\pi x}{a}\sin\frac{3\pi y}{b}}{3\left(\frac{1}{a^2} + \frac{9}{b^2}\right)^2} + \frac{\sin\frac{3\pi\eta}{a}\sin\frac{3\pi\xi}{b}\sin\frac{3\pi u}{2a}\sin\frac{3\pi b}{2b}\sin\frac{3\pi x}{a}\sin\frac{3\pi y}{b}}{9\left(\frac{9}{a^2} + \frac{9}{b^2}\right)^2} \right)$$

(6)

where η, ξ, u, and v are defined in Fig. 10.

The Navier double series solution is a linear, elastic, small-deflection model and is valid under the assumptions of Kirchhoff's hypotheses for plates [22]. Experiments were used to determine the applicability of the Kirchhoff plate theory. Material tests were conducted on silicone rubber with material hardness 55 as per the ASTM D412 standard [23] with straight specimens. Figure 11 shows the normalized deflection as a function of the normalized applied load and marks the loading range that corresponds to the operational range of drip emitters. While the material shows strain softening for large loadings, the behavior of the membrane in the range of interest is linear, justifying the use of the Navier double series solutions to model the bending of the membrane in the emitter. Because the models are linear, they can be superimposed. The total deflection of the membrane w_{bend} before touching the lands is thus given by

$$w_{bend} = w_{uniform} + w_{patch} \tag{7}$$

4.2 Membrane Bending for $P_1 > P_L$. For $P_1 > P_L$, the membrane is in contact with the lands (Fig. 9). The lands exert a contact force w_{conc} on the membrane, constraining the deflection along the lands. After the membrane contacts the lands, the deflection of the membrane is given by

$$w_{bend} = w_{uniform} + w_{patch} + w_{conc} \tag{8}$$

The contact force can be approximated as a partial circular line load applied at the inner land diameter. The deflection profile imposed by a circular line load on a rectangular membrane is asymmetric. To the authors' knowledge, no expressions suitable for modeling the circular lands force as a line load on a rectangular membrane exist in the literature. The line load along the lands was approximated as a series of concentrated loads (Fig. 12). No loads were applied along the width of the channel. Seventy-two concentrated loads were applied along the inner land diameter. Adding additional concentrated loads beyond this number altered the predicted membrane displacement by less than 1%.

The deflection of the rectangular membrane w_{conc} at the point (x_i, y_i) due to a concentrated load F_{lands} at (n_i, m_i) is given by the following expression [22]:

$$w_{conc}(x_i, y_i) = \frac{4F_{lands}}{Dab\pi^4} \left(\frac{\sin\frac{\pi n_i}{a}\sin\frac{\pi m_i}{b}}{\left(\frac{1}{a^2} + \frac{1}{b^2}\right)^2}\sin\frac{\pi x_i}{a}\sin\frac{\pi y_i}{b} + \frac{\sin\frac{3\pi n_i}{a}\sin\frac{\pi m_i}{b}}{3\left(\frac{9}{a^2} + \frac{1}{b^2}\right)^2}\sin\frac{3\pi x_i}{a}\sin\frac{\pi y_i}{b} \right.$$

$$\left. + \frac{\sin\frac{\pi n_i}{a}\sin\frac{3\pi m_i}{b}}{3\left(\frac{1}{a^2} + \frac{9}{b^2}\right)^2}\sin\frac{\pi x_i}{a}\sin\frac{3\pi y_i}{b} + \frac{\sin\frac{3\pi n_i}{a}\sin\frac{3\pi m_i}{b}}{9\left(\frac{9}{a^2} + \frac{9}{b^2}\right)^2}\sin\frac{3\pi x_i}{a}\sin\frac{3\pi y_i}{b} \right)$$

(9)

The deflection at each point (x_i, y_i) of interest along the lands is known based on the geometry of the emitter. Let **n** and **m** be matrices that store the x and y locations, respectively, of each point at which a concentrated load is applied. The vectors designating points at which the displacement is calculated, **x** and **y**, are identical to the vectors designating points at which the concentrated loads are applied, **n** and **m**. At each point (x_i, y_i) along the line load, the total applied line load is the sum of the effects of each concentrated load in the matrix [**n m**]. In a more general case, Eq. (9) could be used to calculate the affect of a series of concentrated loads at position [**n m**] at any point (x, y) in the domain.

The loadings due to the fluid pressure differentials $P_1 - P_2$ and $P_1 - P_a$ cause the membrane to deflect downward. When the membrane makes contact with the inner lands diameter, the line load applied by the lands prevents the membrane from deflecting farther downward. The line load applies a force in the direction opposed to the fluid pressure loading. Since the contact force is acting in the opposite direction as other loads, the values of w_{conc} are negative where the contact between the membrane and the land is made. The magnitude of the applied line load is such that for $P_1 > P_L$, the total deflection at a point (x_i, y_i) along the lands must equal the distance between the surface supporting the membrane and the top surface of the lands h_{land} (Fig. 9), i.e.,

$$h_{land} = \sum_{j=1}^{72} w_{conc}(n_j, m_j)|_{x_i, y_i} + w_{bend}(x_i, y_i) \tag{10}$$
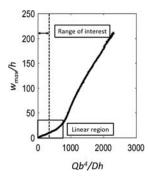
Fig. 11 Dimensionless deflection measurements as a function of dimensionless loading for a rubber tensile test silicone rubber of hardness 55, where Q is the loading applied during the test, w_{max} is the measured maximum deflection, b is the membrane length, D is the flexural modulus of the membrane, and h is the membrane thickness. The range of interest is $(Qb^4/Dh) < 400$, while the linear region extends to $(Qb^4/Dh) < 700$.
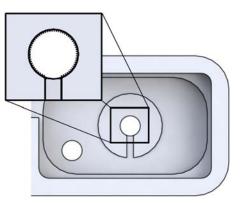

Fig. 12 Contact force between membrane and lands. The contact force between the membrane and the lands was modeled as a series of concentrated forces. Each dot in the dotted line represents a location at which a concentrated force was applied.

The prescribed deflection $h|_{(x_i, y_i)}$ of the membrane at the point (x_i, y_i) due to the concentrated loads is then given by

$$h|_{(x_i,y_i)} = h_{land} - w_{bend}(x_i, y_i) \tag{11}$$

Assuming that the applied force does not vary with the point of application along the lands, the force can be solved for directly using matrix operations. Let $\mathbf{x}$ and $\mathbf{y}$ be 72×1 matrices that store the x and y locations of the points, respectively, along the lands at which the deflection will be constrained. By using Eq. (10), the relationship among the applied force, F_{lands} in Pa m^2, and the known deflection $h_{(\mathbf{x},\mathbf{y})}$ can be written as follows:

$$F_{lands} \cdot \mathbf{W} = \mathbf{h}_{(\mathbf{x},\mathbf{y})} \tag{12}$$

where $\mathbf{W}$ is a 72×1 matrix with units 1/Pa m^3 given by the expression

$$\mathbf{W} = \frac{4}{Dab\pi^4} \left(\sum_{j=1}^{72} \left(\frac{\sin \frac{\pi n_j}{a} \sin \frac{\pi m_j}{b}}{\left(\frac{1}{a^2} + \frac{1}{b^2} \right)^2} \right) \sin \frac{\pi \mathbf{x}}{a} \sin \frac{\pi \mathbf{y}}{b} + \sum_{j=1}^{72} \left(\frac{\sin \frac{3\pi n_j}{a} \sin \frac{\pi m_j}{b}}{3\left(\frac{9}{a^2} + \frac{1}{b^2} \right)^2} \right) \sin \frac{3\pi \mathbf{x}}{a} \sin \frac{\pi \mathbf{y}}{b} \right.$$
$$\left. + \sum_{j=1}^{72} \left(\frac{\sin \frac{\pi n_j}{a} \sin \frac{3\pi m_j}{b}}{3\left(\frac{1}{a^2} + \frac{9}{b^2} \right)^2} \right) \sin \frac{\pi \mathbf{x}}{a} \sin \frac{3\pi \mathbf{y}}{b} \sum_{j=1}^{72} \left(\frac{\sin \frac{3\pi n_j}{a} \sin \frac{3\pi m_j}{b}}{9\left(\frac{9}{a^2} + \frac{9}{b^2} \right)^2} \right) \sin \frac{3\pi \mathbf{x}}{a} \sin \frac{3\pi \mathbf{y}}{b} \right) \tag{13}$$

and $\mathbf{h}_{(\mathbf{x},\mathbf{y})}$ is a 72×1 matrix defined as

$$\mathbf{h}_{(\mathbf{x},\mathbf{y})} = \begin{bmatrix} h|_{(x_1,y_1)} \\ h|_{(x_2,y_2)} \\ \vdots \\ h|_{(x_{72},y_{72})} \end{bmatrix} \tag{14}$$

where the value of each element $h|_{(x_i,y_i)}$ is given by Eq. (11). The value of F_{lands} is then given by

$$F_{lands} = \mathbf{W} \setminus \mathbf{h}_{(\mathbf{x},\mathbf{y})} \tag{15}$$

Because W is a rectangular matrix with more rows than columns, the system is overdetermined, and F_{lands} is the least-squares solution. The backslash operator in Eq. (15) designates the least-squares solution of the matrix system. In this calculation, F_{lands} was assumed to have the same magnitude at each point along the lands. Physically, the value of F_{lands} may vary with the point of application of the force along the circumference of the lands. To evaluate the validity of the solution, the approximated quantity $F_{lands} \cdot \mathbf{W}$ was compared to the known matrix $\mathbf{h}_{(\mathbf{x},\mathbf{y})}$. $F_{lands} \cdot \mathbf{W}$ was found to be within 0.0015% of $\mathbf{h}_{(\mathbf{x},\mathbf{y})}$, validating the analysis methodology. Figure 13 illustrates the deflection of

the membrane due to (1) w_{bend}, (2) Σw_{conc}, and (3) the total bending due to w_{bend} and Σw_{conc} for a representative 2 l/h emitter. The addition of the contact force along the lands changed the shape of the deflection profile. Inside the inner diameter of the lands, the membrane curved upward slightly due to the application of the contact force.

While the expressions derived in this section were applied to a circular line load representing a circular support, the matrix formulations can be applied to a support of generic shape. The expressions are applicable to a line or a patch load of any arbitrary shape along which there is a known deflection applied onto a rectangular membrane. Calculating the magnitude of the line load and the associated deflection analytically allow for a rapid calculation of flow resistance changes with geometry changes.

4.3 Membrane Obstruction Into Channel for $P_1 > P_L$. After the membrane contacts the lands, it begins to deflect into the channel. The total deflection of the membrane is the greatest at the center of the membrane near the outlet of the emitter, where the patch load is applied. As the applied pressure increases, the membrane deforms further into the channel. The deformation of the membrane into the channel effectively increases the length of the channel through which the flow must pass. As the input pressure increases, the cross-sectional area of the flow passage also
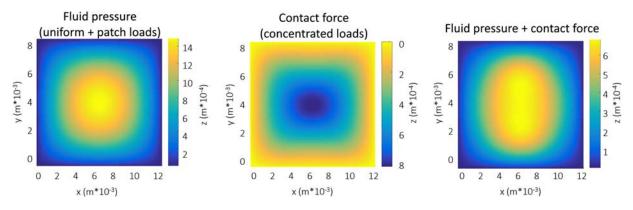
Fig. 13 Bending deflection visualization immediately after the membrane touches the lands in a 2 l/h inline drip emitter. The total force acting on the membrane is the sum of the applied fluid pressure and the contact force exerted by the lands. The inner and outer land diameters of the modeled geometry were 0.0012 m and 0.00476 m, respectively.

decreases. This is the primary source of the increasing flow resistance that causes pressure compensating behavior.

Shamshery et al. [13] previously used the thick beam theory to model the shearing behavior of a section of membrane into the channel of online PC drip emitters. They linearly superimposed the predicted bending and shearing deformations for the thick beam with the bending deformation of the membrane. In our study, the thick beam model was used to provide a cross-sectional profile as a basis to apply correction functions derived from the finite element analysis. The thick beam model alone does not provide an accurate prediction of the magnitude of membrane deflection because the span/depth ratio of the portion of the membrane over the channel is small and the deflection profile is not uniform through the width of the beam (the length of the channel) [24]. This study used the finite element analysis to scale the profile to more accurately model the magnitude of the obstruction.

The finite element model was used to develop functions to describe the magnitude of membrane deformation into the channel and the fraction of the channel into which the membrane deformed as a function of pressure. A mechanical model to study the interaction of the membrane with the lands was constructed in the ANSYS 18.1 static structural package. The membrane was modeled as a first-order Neo-Hookean solid. The model used a rectangular mesh of shell elements with the prescribed thickness. The contact between the membrane and the lands was modeled as frictional with a friction factor of 0.2. Gauss point detection was used between the membrane and the lands structure. For $P_1 < P_L$, the maximum deflection predicted by the finite element model was within 10% of the maximum deflection predicted by Eq. (7).

Shell elements decouple deformation normal to the surface from deformation along the surface. A shell element model of the interactions between the membrane and the lands is an approximation because the channel dimensions are comparable to the thickness of the membrane. Shell elements may underpredict the stiffness of the membrane in the region over the channel after the membrane touches the lands. The model also does not account for the bulk deflection of the membrane in response to the force applied by the lands structure, which may be significant for a membrane of this shape [20]. However, the shell model has significantly lower computational time than other three-dimensional elements. Three-dimensional models of rubbers in the finite element analysis without thin shell approximations are not easily implemented and tend to be error prone [20]. The finite element model captures the changing magnitude and the area of application of the contact force between the lands and the membrane, an interaction not easily modeled using analytical expressions. The finite element model did not model the contact interactions between the channel bottom and the membrane. From experiments, it was known that the bottom of the membrane does not touch the channel within the range of pressures studied. A limiter was applied on the maximum membrane deflection to ensure a channel height of at least 0.01 mm.

The complete system model with fluid–structure interactions was validated using experimental data. The structural model was not validated separately because the experimental data could not be collected on the magnitudes of structural deformation in the channel in the emitter. The approximations in the structural model described above may contribute to the errors in the system model.

In the analysis, the deformation of the membrane is modeled as a constant throughout the thickness of the membrane. For high values of P_1, this may not be true in a real emitter. The deflection of the bottom surface of the membrane, which determines the flow resistance through the emitter, may be less than the deflection of the midplane of the membrane as the contact force increases. Because of these approximations, the finite element model likely overpredicts deformation into the channel for high input pressures.

A nodal pressure $P_1 - P_a$ was applied at the center of the membrane over a circle with diameter equal to the average lands radius, and a nodal pressure $P_1 - P_2$ was applied over the rest of the membrane. P_2 is initially unknown, but it can be calculated iteratively using an initial guess that is refined using the values calculated from the complete hybrid model, which iterates over the calculated pressures and structural deformation.

Due to the high flow resistance in pressure compensating emitters, $P_1 - P_2$ was expected to be approximately an order of magnitude lower than P_1 for $P > P_{act}$ or on the order of 0.1 bar. Thus, the first iteration of the finite element model was run with $P_1 - P_2$ equal to 0.1 bar. The resulting scaling functions were used in the complete hybrid model to calculate Q, as well as a new prediction for the value of P_2 at each input pressure. The new P_2 predictions were then used as inputs in another run of the finite element model. This process was repeated until further refinements on the values of P_2 had no affect on the predicted flow rate Q. After two iterations of the finite element model, the final predicted values of Q for the 2 l/h emitter converged with relative error between iterations of less than 5% (Fig. 14).
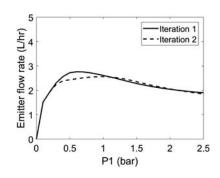

Fig. 14 The predicted flow rate of the 2 l/h emitter converged within two iterations of the scaling functions over P_2
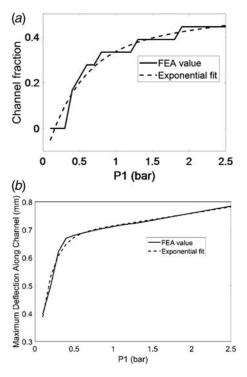
Fig. 15 Scaling functions describing membrane obstruction into channel. Exponential functions were fit to results from the FEA model to create expressions for a scaling factor and percent channel shearing as a function of the pressure. The scaling functions at the final iteration for the 2 L/hr emitter geometry are shown here. (*a*) The channel fraction, or percentage of the channel into the which the membrane had sheared, at each input pressure. (*b*) The maximum deflection along the channel at each input pressure.

The deflection of the membrane in the finite element model was sampled at 0.1-mm increments along the length of the channel and used to determine the fraction of the channel covered by the membrane. This fraction rose with P_1 over the entire pressure range (Fig. 15). The pressure at which the membrane made contact with the lands corresponds to a marked change of slope in the maximum deflection along the channel as a function of pressure.

Exponential functions were fit to describe the maximum deflection and channel fraction as a function of P_1. The maximum deflection into the channel $w_{ch,max}$ was used to scale a normalized deflection profile for a clamped thick beam [25],

$$
\begin{aligned}
w_{normalized}(x) = (2.3269 \times 10^{14})x^4 - (2.3269 \times 10^{11})x^3 \\
+ (5.6525 \times 10^7)x^2 + 824.2173x - 0.0077
\end{aligned}
\tag{16}
$$

The deflection along the length of the channel decayed parabolically from its maximum value at the inner land radius l_{ri}. A parabolic function $S_p(y)$ was defined with a value of 1 at the inner land diameter and a value of 0 at the point where the membrane first contacts the lands, as defined by the channel fraction. The scaling function $S_p(y)$ gives the ratio of the deflection at a given point along the channel to the maximum deflection along the channel for a constant input pressure P_1. Thus, the deflection profile into the channel (Fig. 16) w_{ch} at a given point along the channel y is given by

$$
w_{ch}(x) = (w_{ch,max} - h_{lands}) \times S_p(y) \times w_{normalized}(x)
\tag{17}
$$

where h_{lands} was subtracted from $w_{ch,max}$ to compute the deflection into the channel with respect to the lands.

The exponential fit functions for the maximum deflection along the channel and channel fraction as a function of input pressure (Fig. 15) were generated using increments of 0.1 bar for P_1 and have R^2 values of 0.99 and 0.96, respectively. Sampling at 0.1 bar intervals between 0.2 and 0.6 bar and 0.4 bar intervals between 0.6 and 2.2 bar did not lower the R^2 value of the fit functions, but reduced the required computational time by approximately 60%. A higher sampling resolution was used for lower pressures where the maximum deflection changes more rapidly. The scaling functions for the 1.1 l/h and 3.8 l/h emitters were found using this sampling method.

To find the scaling factors for the 1.1 and 3.8 l/h emitters, the final values for P_2 from the 2 l/h emitter analysis were used in the first iteration of the new finite element analysis. Due to the more accurate initial input for P_2, compared to the initial values of 0.1 bar used for the 2 l/h emitter, the flow rate predicted by the hybrid model for the 1.1 l/h emitter and the 3.8 l/h emitter converged with one iteration of scaling functions from the finite element analysis.
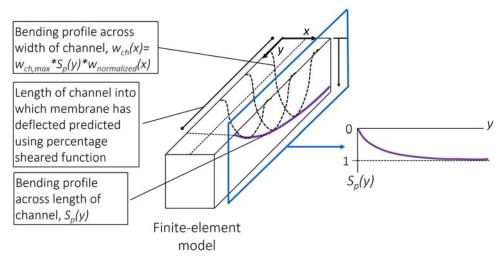

Fig. 16 The hybrid-analytical model incorporates results from FEA simulations using scaling relationships. The maximum deformation of the membrane into the channel and the length of the channel into which the membrane has deformed are predicted from FEA simulations using scaling relationships (Fig. 15). The profile across the width of the beam $w_{normalized}(x)$ is found from Eq. (16).

5 Flow Modeling

When the flow enters the section under the membrane, there are two paths that it can take to reach the channel, flow paths A and B, as shown in Fig. 17(a). Due to the much longer flow path, the flow resistance through the flow path B is much higher than the resistance through A, and therefore flow through the flow path B was neglected in this analysis. Path A can be subdivided into two zones, as shown in Fig. 17(b).

The height of the passage in zone 1 was calculated using the analytical expressions for membrane bending (Eqs. (7) and (8)). The height of the passage in zone 2 was calculated using the functions derived from the finite element analysis, as per Eq. (17). Zone 1 was divided into 10 subsections, and zone 2, the dominant flow resistance, was divided into 50 subsections. The profile of the membrane bending across the width of the section (the dimension parallel to the membrane width b) was calculated in each section, and a polynomial was fit to match the bending profile. The hydraulic diameter in each subsection was calculated by integrating to find the area through each section and the perimeter enclosing each subsection. The frictional loss in each subsection was calculated using Eq. (18). The frictional losses through a duct are given by

$$K_{fric} = \frac{fL}{D_h} \qquad (18)$$

In this expression, f is the friction factor, L is the length of the duct, and D_h is the hydraulic diameter of the duct. The total frictional loss is equal to the sum of the frictional loss in each subsection. The variables D_h and f depend on the cross-sectional profile and area of the duct and were calculated by integrating along the duct profile, defined by the expressions for the bending and shearing of the membrane described earlier. The parameter f was calculated implicitly using the Colebrook interpolation formula [26] using an absolute roughness of 0.0015 mm, estimated from the literature for drawn plastic pipes [27,28],

$$\frac{1}{f^{1}/2} = -2.0 \log \left(\frac{\epsilon/D_h}{3.7} + \frac{2.51}{Re_{D_h} f^{1}/2} \right) \qquad (19)$$
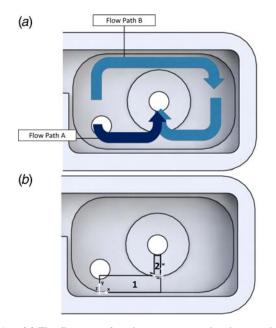

(a)

(b)

Fig. 17 (a) The flow entering the passage under the membrane can go through the path A or path B. Because flow resistance through the path B is much higher than the flow resistance through the path A, the flow resistance of the path B was neglected in the analysis. (b) The flow resistance through the flow path A was calculated as the sum of the flow resistances in zones 1 and 2.

The flow velocity can be calculated using the properties of the fluid and the losses through the channel [13,26] by using

$$P_2 - P_a = \frac{1}{2} \rho K_{fric}(v_{ave})^2 + \frac{1}{2} \rho (v_{ave})^2 \Sigma K_{minorloss} \qquad (20)$$

$K_{minorloss}$ are the minor loss coefficients for irregularities in the flow path geometry. In this model, minor losses for the flow moving out of the labyrinth into the chamber underneath the membrane and through the outlet were accounted for. The magnitude of $K_{minorloss}$ depends on the diameters of the passageway before and after the change in duct dimension and can be estimated using the expression [26]:

$$K_{minorloss} = \left(1 - \frac{D_1^2}{D_2^2} \right)^2 \qquad (21)$$

Equation (20) was derived from the Navier–Stokes solution for one-dimensional, steady-state, fully developed flow. Due to the varying dimensions of the flow path, the flow through the emitter paths is neither one dimensional nor fully developed. These expressions can be used as a reasonable approximation where locally fully developed flow can be assumed. Following [29], the approximation for locally fully developed flow is reasonable when the Navier–Stokes equations can be reduced to

$$\frac{\delta P}{\delta x} = \mu \frac{\delta^2 U}{\delta z^2} \qquad (22)$$

$$\frac{\delta P}{\delta y} = 0 \qquad (23)$$

$$\frac{\delta P}{\delta z} = 0 \qquad (24)$$

A self-consistency check was performed after evaluating the flow rate using Eq. (20) at input pressures of 0.1 and 1 bar. For the locally fully developed flow assumption to be valid, the relative magnitude of the neglected terms must be small in comparison to the retained terms when moving to Eqs. (22)–(24). The time-dependent term in the Navier–Stokes equation is negligible because the flow is steady state at each input pressure. In zone 1, it was estimated that the flow velocity in the y direction (Fig. 17) was on the order of one-tenth of the flow along the x direction, because the flow resistance through the flow path B was approximately ten times the flow resistance through the flow path A. The order of the flow velocity in the y direction was found using the calculated flow rate out of the emitter and the average flow path dimensions. Conservation of mass was used to estimate the order of the flow velocity in the z direction.

The self-consistency check suggested that the approximation of locally fully developed flow was most valid in zone 2 for $P > P_L$. Inertial contributions of the flows in the x and z directions could be significant, particularly in zone 1. Because the flow resistance through zone 2 is significantly higher than the flow resistance through zone 1, deviations from the approximation of locally fully developed flow in zone 1 will introduce less error in the analysis. The analysis suggested that the approximation of locally fully developed flow can be used to analyze the relative flow behavior through emitters of different geometries, but it may result in some error in the model, particularly for low pressures.

6 Results

The hybrid computational–analytical model was used to predict the flow rate as a function of pressure for three models of the Turbo Cascade PC emitter (1.1, 2.0, and 3.8 l/h). The emitter flow rates as a function of pressure were measured by attaching samples of the drip tubing to an adjustable pressure water source. Pressure and flow rate were measured as described in Sec. 2. Figure 18 compares
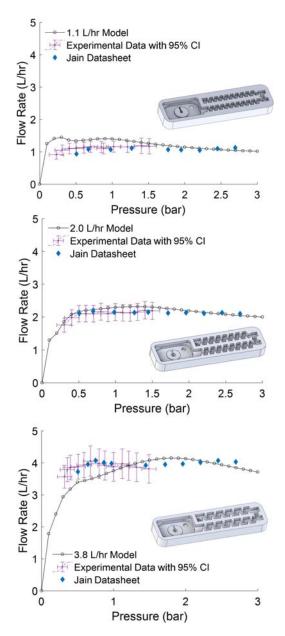
Fig. 18 The flow rate behavior as a function of pressure as predicted by the hybrid computational–analytical model and the experimental data collected by the authors. The solid line shows the model predictions, with circles denoting individual data points. The dashed line shows experimental data, with crosses denoting individual data points. The diamonds are the published datasheet values [30]. The CAD model shown with each plot is of the corresponding emitter.

Table 2 Summary of calculated average flow rate and activation pressure for each emitter, using model predictions and experimental data over the range 0–1.5 bar

	1.1 l/h Emitter	2.0 l/h Emitter	3.8 l/h Emitter
Average flow rate: model (l/h)	1.38	2.09	3.47
P_{act}: model (bar)	0.10	0.30	0.35
Average flow rate: experiment (l/h)	1.12	2.10	3.87
P_{act}: experiment (bar)	0.30	0.30	0.30

regime of the 1.1 l/h emitter has flows with the lowest Re number, where the models used will be least accurate because of the possible laminar flow. These effects may account for the comparatively larger errors (maximum 35% at low pressure) in the flow rate predicted by the model for the 1.1 l/h emitter.

The model was consistent with the experimental data for the 2.0 and 3.8 l/h emitters over most of the tested pressure range. The flow rate predicted by the model was reasonably close to the datasheet values published by Jain Irrigation Ltd. for the 1.1 l/h emitter and was very close to the published values for the 2.0 and 3.8 l/h emitters. The trends shown in the model match the trends of the experimental data. For the 1.1 l/h emitter, the average error between the model and the experimental data was 10.7%, and the average error between the model and the datasheet values was 18.1%. For the 2.0 l/h emitter, the average error between the model and the experimental data was 4.7% and the average error between the model and datasheet values was 6.7%. For the 3.8 l/h emitter, the average error between the model and the experimental data was 11.0% and the average error between the model and the datasheet values was 8.9%.

The activation pressure of an emitter was defined as the pressure at which the flow rate was within 10% of the average flow rate. The calculated activation pressures and average flow rate are presented in Table 2. For consistency with the available experimental data set, the activation pressure predicted by the model was calculated for the range 0–1.5 bar. The model predicted the flow rate through each emitter over the range of pressures and the activation pressure of each emitter with reasonable accuracy.

Experimental data were collected to confirm the accuracy of the published data and to determine the confidence interval. The 95% confidence interval of the experimental data was consistent with the published data, indicating that the published data should be sufficient to validate the predicted model flow rate. The experimental data were used to evaluate the accuracy of the predicted activation pressure because the activation pressure in the published data is reported with a unknown safety factor. The published minimum operating pressure is 0.5 bar for all three emitters [30].

The model had higher fidelity for emitters with higher flow rates. Similar absolute errors between the model predictions and the experimental and datasheet curves were similar for all emitters; this led to larger relative errors for lower flow rates. Overall, the model has sufficient accuracy to characterize the relative performance of drip emitters given a defined architecture over a range of flow rates.

the measured flow rates as a function of pressure to the hybrid model predictions, indicating 95% confidence intervals for measured values. The figure also shows the geometry of each emitter. As a comparison, the data provided in the product datasheet by Jain Irrigation Ltd. [30] are also included.

The model overpredicted the experimental data for the 1.1 l/h emitter, particularly at low pressures. Because the dimensions in the pressure compensating chamber of the 1.1 l/h emitter are the smallest, any errors in the predicted membrane deformation will have a magnified effect on the predicted flow rate. In addition, the hybrid modeling approach approximated turbulent flow at all design points because the flow was expected to be turbulent at the majority of points and because the transition number is highly geometry dependent and difficult to predict. The low-pressure

7 Discussion

The behavior of P_2 can provide some insight into the behavior of a drip emitter. For a given P_1, the corresponding value of $P_1 - P_2$ is much smaller than the magnitude of P_1. Changes in P_1 also result in comparatively smaller corresponding changes in the quantity $P_1 - P_2$ (Fig. 19). Thus, $P_1 - P_2$ can be approximated as a constant Δ_p. Because the change in the uniform pressure loading $P_1 - P_2$ is much smaller than the corresponding change in P_1, the flow resistance before the channel does not contribute to the pressure compensating behavior (Eq. (7)).
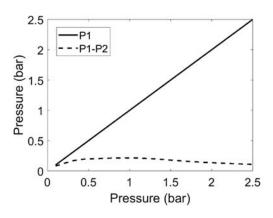
Fig. 19 P_2 can be predicted by approximating $P_1 - P_2$ as a constant Δ_p because changes in $P_1 - P_2$ are much smaller than corresponding changes in P_1

The value of Δ_p depends on the geometry of the emitter. For the 2 l/h emitter, for $P_1 > P_L$, Δ_p is 0.17 bar with a standard deviation of 0.037 bar. For the 1.1 l/h emitter, Δ_p is 0.053 bar with a standard deviation of 0.016 bar. For the 3.8 l/h emitter, Δ_p is 0.41 bar with a standard deviation of 0.071 bar. This relationship can be used to decrease the computational time of the hybrid model. For a given geometry, the number of iterations needed for the model to converge can be reduced by first evaluating the hybrid model at an intermediate value of P_1, then estimating the constant Δ_p, and finally using the relationship $P_2 = P_1 - \Delta_p$ to guess an initial value of P_2 for each design point. Δ_p is a seed value used to increase convergence speed; it does not constrain the predicted value of P_2 and can be used when modeling emitters that do not have perfect PC behavior.

The hybrid computational–analytical model captured the pressure compensating behavior and flow rate for three distinct emitter geometries. The model has a much wider range of applicability than published analytical models, in that it accounts for the flow behavior through tortuous paths and asymmetrical flow channels. The hybrid model has improved accuracy when compared to a purely analytical model [13].

The model makes some simplifications that likely contribute to the small inaccuracies apparent in Fig. 18. In the analytical model, the contact force between the membrane and the lands is approximated as a series of concentrated loads; however, the contact is actually a continuous distributed load applied over an increasing area. In the finite element model, the mesh is composed of two-dimensional shell elements and assumes that the midplane deflection of the membrane is equal to the deflection of the bottom surface of the membrane. The analytical expressions for the flow assume locally fully developed flow although a self-consistency check suggested that the flow may deviate from this behavior. The analysis of locally developed flow suggested that the flow models would have higher error at lower pressures, which is consistent with the results shown in Fig. 18.

The computational time required to fully model an emitter makes model-based design optimization extremely time and resource intensive. Generating the high-resolution CFD model predictions for a given path geometry such as those presented in Fig. 6 took 4–6 h using five 2.4 GHz Intel Xeon Processor cores in parallel, depending on the geometry of the path. Modeling the contact between the membrane and the lands and coupling the fluid–structure interactions in a computational model would increase this time significantly more. By using the same processor, the hybrid computational–analytical model with simplifying assumptions presented herein can generate predictions of similar resolution in approximately 30 min. This efficiency enables a level of iteration and optimization of emitter designs that would not be possible using other modeling approaches.

8 Conclusions

CFD and FEA are powerful but computationally intensive methods of modeling the behavior of inline drip emitters. Their long processing time makes it difficult to optimize the designs of drip emitters with tortuous paths and complex geometries.

Prior modeling approaches for pressure compensating valves have been time intensive or have had limited applicability. Using a hybrid computational–analytical model significantly reduces the computational time required to model and optimize the behavior of PC inline drip emitters while maintaining a high level of accuracy. The model and techniques presented in this paper can be used to model a wide range of geometries. In the future, this method could be used to improve the design of inline drip emitters to lower activation pressure and material costs associated with manufacturing the emitter. Lowering the activation pressure could reduce the energy costs associated with operating a drip irrigation system using the emitters.

The hybrid modeling approach uses analytical models that can be solved easily and accurately, in combination with parameters extracted from computational models to describe complex physics, which cannot be easily described analytically. The presented approach could be applied to other systems, where the physics of parts of the system are easily modeled analytically. A hybrid approach allows for accurate modeling of complex physical phenomena, but expends intensive computational effort only when necessary. The model described in this paper provides an example of defining key interfaces between analytical and computational models, allowing both approaches to be used in combination.

In the future, the model could be used for design optimizations of inline emitters. For example, the hybrid model could enable fast iteration through land geometries to minimize the activation pressure for a chosen tortuous path geometry. Additional work on PC drip emitter modeling could include improving the fidelity of the flow model by determining how geometric features in the flow path contribute to the transition of laminar to turbulent flow and including inertial effects in the flow model, validating a refined structural model, adapting the methods to more general pressure compensating systems for applications outside irrigation, and developing a model to analytically predict the flow behavior through a variety of alternate path geometries.

Nomenclature

a = membrane length (m)
b = membrane width (m)
f = friction factor
h = membrane thickness (m)
m = y-coordinate of concentrated load (m)
n = x-coordinate of concentrated load (m)
q = loading applied during tension test of silicone rubber (Pa)
u = width of patch load (m)
v = length of patch load (m)
D = flexural modulus of membrane (Pa m^3)
E = Young's modulus of membrane (Pa)
G = shear modulus of membrane (Pa)
L = characteristic flow passage length (m)

U = characteristic flow passage velocity parallel to passage length (m)

V = characteristic flow passage velocity perpendicular to passage length (m)

h_p = characteristic flow passage height (m)

h_{land} = distance between the surface on which the membrane rests and the top of the lands (m)

l_{ri} = inner land radius (m)

v_{ave} = average flow velocity in duct (m)

w_{bend} = total deflection of membrane before touching the lands (m)

$w_{ch}(x)$ = deformation profile of membrane across width of channel (m)

$w_{ch,max}$ = maximum deformation of membrane into channel (m)

w_{conc} = deflection of membrane due to a concentrated load (m)

w_{max} = maximum deflection measured during tension test with silicone rubber (m)

$w_{normalized}(x)$ = normalized deflection profile for a clamped thick beam (−)

$w_{uniform}$ = deflection of membrane due to uniform load (m)

D_h = hydraulic diameter (m)

F_{lands} = magnitude of concentrated load (N)

H_A = membrane hardness (shore A)

K_1 = flow resistance parameter through the tortuous path, relating P_1 and P_2

K_{fric} = frictional losses through duct

$K_{minorloss}$ = minor loss coefficient

K_{mt} = total flow resistance underneath the membrane

P_1 = pressure above membrane; input pressure from pipe (Pa)

P_2 = pressure under membrane; pressure at the end of the tortuous path (Pa)

P_a = atmospheric pressure (Pa)

P_L = pressure at which membrane contacts the lands (Pa)

Re_{D_h} = Reynolds' number of flow with respect to hydraulic diameter (−)

$S_p(y)$ = ratio of the deformation at a coordinate along the channel to the maximum deflection in the channel (m)

ε = absolute roughness of emitter material (−)

η = vertical distance to center of patch load (m)

ν = Poisson's ratio of membrane

ρ = density of water (kg/m^3)

τ = characteristic time describing the flow (s)

ξ = horizontal distance to center of patch load (m)

References

[1] United Nations Enviornment Programme, 1998, "Sourcebook of Alternative Technologies for Freshwater Augmentation in some Countries in Asia," Technical Report.

[2] Phansalkhar, S., and Verma, S., 2008, *Silver Bullets for the Poor: Off the Business Park*. IWMI-Tata Water Policy Program.

[3] Woods Institute for the Environment, 2008, "An Alternative Development Model? Assessing Solar Electrification for Rural Development in Benin," Stanford University, https://woods.stanford.edu/research/funding-opportunities/environmental-venture-projects/alternative-development-model-assessing-solar-electrification-income

[4] Food and Agricultural Organization, 2018, "The Benefits and Risks of Solar-Powered Irrigation—a Global Overview," http://www.fao.org/3/i9047en/I9047EN.pd

[5] Shamshery, P., and Winter, A. G., 2017, "Shape and Form Optimization of Online Pressure Compensating Drip Emitters to Achieve Lower Activation Pressure," J. Mech. Design, **140**(3), 035001.

[6] Jain Irrigation Ltd., Jalgao, India, 2016, private communication.

[7] Glaad, Y., 1974, "Hydraulic and Mechanical Properties of Drippers," Proceedings of the Second International Drip Irrigation Conference.

[8] Palau-Salvador, G., Aryiza-Valverde, J., and Bralts, V., 1974, "Hydraulic Flow Behavior Through an In-Line Emitter Labyrinth Using CFD Techniques," ASAE.

[9] Dazhuang, Y., Peiling, Y., Shumei, R., Yunkai, L., and Tingwu, X., 2007, "Numerical Study on Flow Property in Dentate Path of Drip Emitters," New Zealand J. Agric. Res., **50**(5), pp. 705–712.

[10] Wei, Q., Shi, Y., Dong, W., Lu, G., and Huang, S., 2006, "Study on Hydraulic Performance of Drip Emitter by Computational Fluid Dynamics," Agric. Water Manage., **84**, pp. 130–136.

[11] Brown, A., Shi, Y., Marzo, A., Staicu, C., Valverde, I., Beerbuam, P., Lawford, P., and Hose, D., 2012, "Accuracy vs. Computational Time: Translating Aortic Simulations to the Clinic," J. Biomech., **45**, pp. 516–523.

[12] Lau, K. D., Daiz, V., Scambler, P., and Burriesci, G., 2010, "Mitral Valve Dynamics in Structural and Fluid-Structure Interaction Models," Med. Eng. Phys., **32**, pp. 1057–1064.

[13] Shamshery, P., Wang, R., and Tran, D. V., 2017, "Modeling the Future of Irrigation: A Parametric Description of Pressure Compensating Drip Irrigation Emitter Performance," PlosOne, **12**(4), e0175241.

[14] Zhengying, W., 2013, "The Step-by-Step CFD Design Method of Pressure-Compensating Emitter," Eng. Sci., **11**, pp. 62–67.

[15] Wang, W., Bralts, V., and Wang, J., 2012, "A Hydraulic Analysis of an Online Pressure Compensating Emitter Using CFD-CSD Technology," ASAE Annual International Meeting, Dallas, TX, July 29–Aug. 1.

[16] ANSYS, 2018, *Ansys Modeling Guide: The K-Omega and SST Models*, Canonsburg, PA.

[17] Nishimura, T., Bian, Y., Matsumoto, Y., and Kunitsugu, K., 2003, "Fluid Flow and Mass Transfer Characteristics in a Sinusoidal Wavy Walled Tube at Moderate Reynolds Number for Steady Flow," Heat Mass Transf., **39**(3), pp. 239–248.

[18] Dai, Z., Fletcher, D. F., and Haynes, B. S., 2015, "Influence of Tortuous Geometry on the Hydrodynamic Characteristics of Laminar Flow in Microchannels," Chem. Eng. Technol., **38**, pp. 1406–1415.

[19] Yongxin, L., Guangyong, L., Xiangyu, Q., Jiandong, W., and Alam, M., 2005, "Computational Fluid Dynamics Analysis and Verification of Hydraulic Performance in Drip Irrigation Emitters," Irrigation Association International Irrigation Technical Conference.

[20] Gent, A. N., 2012, *Engineering With Rubber: How to Design Rubber Components*, 3rd ed., Hanser Publications, Germany.

[21] ASTM International, 2016, "Designation d2240-15: Standard Test Method for Rubber Property—Durometer Hardness," https://www.astm.org/Standards/D2240

[22] Ventsel, E., and Krauthammer, T., 2001, "Rectangular Plates," *Thin Plates and Shells: Theory, Analysis, and Applications*. Marcel Dekker Inc., New York, pp. 55–104.

[23] ASTM International, 2016, "Designation d412-15a: Standard Test Methods for Vulcanized Rubber and Thermoplastic Elastomers - Tension," http://www.astm.org/DATABASE.CART/HISTORICAL/D412-15A.htm

[24] Young, W., and Budynas, R. G., 2002, "Beams: Flexure of Straight Bars," *Roark's Formulas for Stress and Strain*, McGraw-Hill, New York, pp. 125–188.

[25] Ghugal, Y. M., and Sharma, R., 2011, "A Refined Shear Deformation Theory for Flexure of Thick Beams," Lat. Am. J. Solids Struct., **8**(2), pp. 183–195.

[26] White, F., 1998, "Viscous Flow in Ducts," *Fluid Mechanics*, J. P. Holman, and J. Lloyd, eds., McGraw-Hill, New York, pp. 325–405.

[27] McGovern, J., 2011, "Technical Note: Friction Factor Diagrams for Pipe Flow," Dublin Institute of Technology, *Technical Report*.

[28] Pipeflow Fluid Thinking Software Solutions, 2012, "Pipe Roughness," https://www.pipeflow.com/pipe-pressure-drop-calculations/pipe-roughness

[29] Sonin, A. A., 2002, "Criteria for Locally Fully Developed Viscous Flow," *MIT Fluid Mechanics Course Materials*, MIT OpenCourseWare

[30] Jain Irrigation Systems Ltd., 2016, "Jain Turbo Cascade PC, PCNL, and PCAS," http://www.jains.com/irrigation/emitting%20pipe/turbo%20cscade%20pc%20pcnl%20pcas.htm